Passband broadening of sub-wavelength resonator-based glide-symmetric SIW filters

Javier Martínez[(1)], Ángela Coves[(1)],

Francisco Mesa[(2)] and Óscar Quevedo-Teruel[(3)]

javier.martinez35@alu.umh.es, angela.coves@umh.es,

mesa@us.es, oscarqt@kth.se

[(1)]Dpto. de Ingeniería de Comunicaciones-I3E,

Universidad Miguel Hernández de Elche, 03202 Elche, Alicante

[(2)]Dept. of Applied Physics 1, ETS de Ingeniería Informática,

Universidad de Sevilla, Seville, Spain

[(3)]Division of Electromagnetic Engineering,

KTH Royal Institute of Technology, 114 28 Stockholm, Sweden

Abstract

Here, we discuss the virtues of glide symmetry for designing low-frequency band-pass periodic filters in substrate integrated waveguide (SIW) technology based on complementary split-ring resonators (CSRRs). Conventional (non-glide) versions of these filters have a narrow passband, due to the fact that this band is below the cutoff frequency of the background waveguide. When glide symmetry is added to the filter configuration, the low-frequency passband is significantly widened, as well as the first stopband. The dispersion properties of both conventional and glide-symmetric periodically loaded waveguides are analyzed and compared with commercial software and an equivalent circuit model. Finally, two prototypes of the proposed glide-symmetric structure have been designed and built, illustrating the potential of this technique to widen the passband and reduce insertion losses of conventional sub-wavelength CSRR-loaded SIW filters.

I. Introduction

Periodic waveguiding structures have attracted a lot of interest among microwave engineers due to their slow-wave and passband/stopband characteristics [1]. These characteristics have been used for size reduction [2], [3] and rejection band improvement [4], [5]. Periodic

structures can possess additional higher symmetries [6], which provides useful supplementary features. These special periodic structures, in their 1-D configuration, were first studied in the 1960's and 1970's through the generalized Floquet theorem [7].

One relevant type of higher symmetry is glide symmetry, which is created with a combination of a translation and mirroring over a plane [8]. This symmetry has recently been used to reduce the dispersion of conventional periodic structures [9], and has advantageously been used to produce broadband lens antennas [10]. Glide symmetries are also able to increase the equivalent refractive index of periodic structures [11], [12] as well as the bandwidth and attenuation constant of electromagnetic band gaps [13]. Other researchers have also attempted to broaden stopbands by means of metamaterials [14], [15]. Stopbands have been employed to produce cost-effective fully metallic gap waveguides [16], [17], flanges [18] and filters [19]. Additionally, glide symmetry allows for an increase of the anisotropy contrast of periodic structures [20] and their magnetic responses [21]. These properties can be used to compress lenses [20], for example with transformation optics, or to reduce the reflections at their contour [21].

It is worth noting that, to produce an operational difference with respect to conventional periodic structures, the constituent shifted sub-cells of a glide-symmetric unit cell have to be strongly coupled, which implies short electric distances between sub-cells [22]. Therefore, when using any approximate approach to study glide-symmetric structures, such as the equivalent circuit proposed in this work, the mutual coupling between sub-unit cells has to be well accounted for [23].

In this paper, we prove that glide symmetry is able to increase the bandwidth of operation of a substrate integrated waveguide (SIW) operating below cutoff frequency. In particular, we study and compare the transmission/reflection response and dispersion characteristics of a SIW loaded with complementary square split-ring resonators (CSRRs) [24]–[26] with and without glide symmetry [see Fig. 1]. First, a physically-based equivalent circuit model of the structures is discussed, which is able to explain in simple terms its operation and the differences between conventional and glide operations. Second, the full-wave simulator is used to accurately study the dispersion properties of the structures and to extract useful information for the practical implementation of the filters. Finally, in order to validate the potentialities of our proposal, a low-frequency pass-band filter is designed and built based on the proposed glide-symmetric CSRR-etched structure. The experiments show a clear improvement in bandwidth and insertion losses with respect to similar sub-wavelength filter
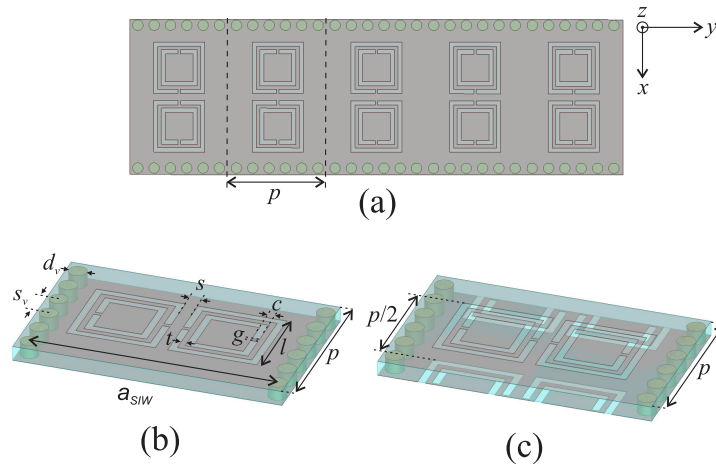
Fig. 1. (a) Top view of a SIW periodically etched with two rows of CSRRs. Unit cell of a periodic SIW with a pair of face-to-face (2-sided) CSRRs etched on (b) the top waveguide metallic surface [conventional structure], and (c) on both waveguide metallic surfaces with glide symmetry.

topologies reported in the technical literature that employ resonators to produce evanescent-wave transmission.

It is worth mentioning that the advantages of using glide symmetry are not exclusive for the specific case studied in this paper. In fact, glide symmetry can be used complementary to the majority of the techniques existing in the literature.

II. EQUIVALENT CIRCUIT MODEL

A. *Derivation of the topology and circuit parameters*

Our aim in this section is to find a simple physically-based equivalent circuit that models a SIW section below cutoff when loaded with CSRRs. In order to keep the circuit model as simple as possible, we assume a rectangular waveguide of width a [27] filled with a dielectric material and only one row of periodic CSRRs, as illustrated in Fig. 2(a). The corresponding unit cells (period p) without and with glide symmetry are shown in Figs. 2(c) and (d), respectively. These simplified unit-cell versions of the structures in Fig. 1 will conveniently account for the main characteristics of the physical performance of the filters. The presence of two rows of CSRRs will certainly enhance the passband bandwidth [25], [26], [28] but will also complicate the circuit model, hindering the effects of higher symmetries in the structure. The physical insight provided by this circuit model will allow us to better understand the evanescent-wave transmission behaviour of the structure, and then to exploit this knowledge for practical applications in the following sections.
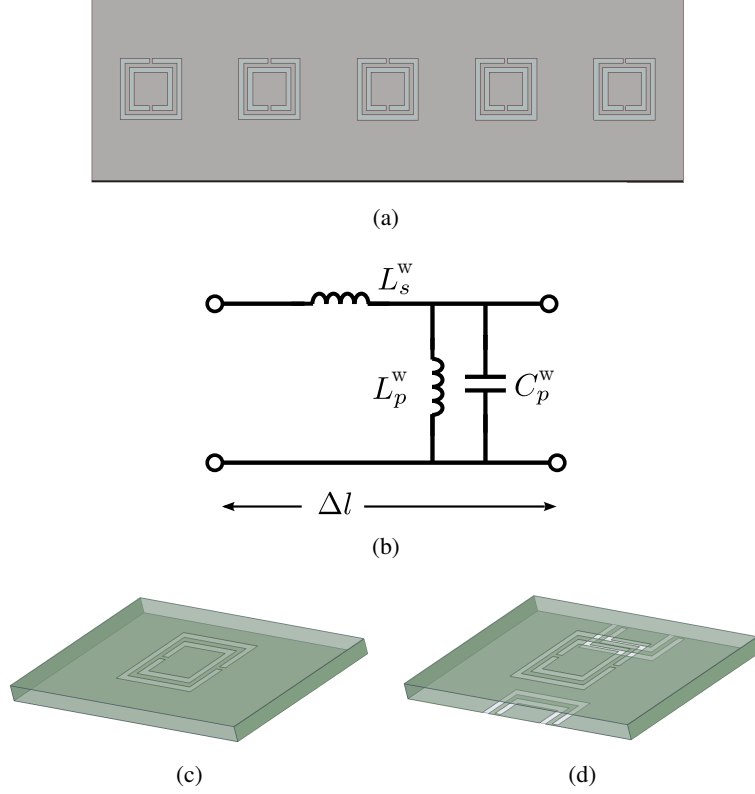
Fig. 2. (a) Top view of a rectangular waveguide filled with dielectric and periodically etched with one row of CSRRs. (b) Equivalent circuit model of a section of rectangular waveguide of length Δl working below the cutoff frequency of the TE$_{10}$ mode. (c) Conventional (no-glide) unit cell of the etched waveguide. (d) Glide-symmetric unit cell of the etched waveguide.

The specific dimensions employed in this section for the rectangular waveguide are $a = 10\,\text{mm}$, $b = 0.86\,\text{mm}$, and $\varepsilon_r = 2.55$ (corresponding to the substrate Taconic TLX8), which set the cutoff frequency of the waveguide at $10.92\,\text{GHz}$. Following the derivations in [29], [30], a section of length Δl of the unloaded metallic waveguide working below cutoff is modelled as shown in Fig. 2(b) for TE$_{10}$-mode operation. The circuit parameters are given by [3], [29], [30]

$$L_s^{\text{w}} = \mu_0 \Delta l \tag{1}$$

$$L_p^{\text{w}} = \frac{\mu_0 a^2}{\pi^2 \Delta l} \tag{2}$$

$$C_p^{\text{w}} = \varepsilon_0 \varepsilon_r \Delta l \ . \tag{3}$$

In order to obtain a relatively simple equivalent circuit of the unit cell in Fig. 2(c,d) in terms of only *lumped* elements, the unit cell of length p is split into four electrically-short sub-sections of length $\Delta l = p/4$ coupled to a *single* square CSRR etched on the top wall of the waveguide. Starting from the theoretical model given in (1)–(3), each sub-section of the

etched waveguide in evanescent regime is then modelled as

$$L_s = \xi_s L_s^{\mathrm{w}} \quad , \quad L_p = \xi_p L_p^{\mathrm{w}} \quad , \quad C_p = \xi_p C_p^{\mathrm{w}} \tag{4}$$

with ξ_s and ξ_p being factors that will take into account the deviation of the etched-waveguide subsection with respect to the theoretical rectangular-waveguide one.

The circuit modeling of the CSRR is a $L_R C_R$ tank, as shown in the yellow highlighted area of Fig. 4(a). For the case of a CSRR in a microstrip line, the corresponding values of the capacitance and inductance (say, L_m and C_m), as well as the resonance frequency, of the CSRR were derived in [24]. These results are directly employed here with a correcting factor ν that should be slightly adjusted in each case; namely,

$$L_R = L_m/\nu \qquad , \qquad C_R = \nu C_m . \tag{5}$$

The study of the coupling of the CSRR to the waveguide gives as result that this coupling is of magnetic nature, and thus it is accounted for the four inductive couplings illustrated in the equivalent circuit of Fig. 4(a) with a coupling factor k_{RW}. Although, to the authors' knowledge, there is no closed-form expression for this parameter, its value is not expected to be very different from 1 (namely, total magnetic influence). The geometrical parameters of the square CSRR, defined in Fig. 1(b), are set for all the cases in this work as $l = 3.92\,\mathrm{mm}$, $c = 0.32\,\mathrm{mm}$, $s = 0.54\,\mathrm{mm}$, $t = 0.26\,\mathrm{mm}$, and $g = 0.18\,\mathrm{mm}$. According to [24], the initial values of the inductance and capacitance of the CSRR are $L_m = 1.68\,\mathrm{nH}$ and $C_m = 0.4\,\mathrm{pF}$, which have to be modified in our case by a factor $\nu = 1.33$ to give finally $L_R = L_m/\nu = 1.26\,\mathrm{nH}$ and $C_R = \nu C_m = 0.52\,\mathrm{pF}$. These values will be employed in all the three different cases analyzed next.

When more than one CSRR is etched on the waveguide walls, as in the structures shown in Figs. 2(a) or (d), there will be electromagnetic coupling between the CSRRs. The nature of this coupling can be studied by following the procedure reported in [23], [31]; namely, checking how the coupling coefficient of a pair of resonators,

$$k = \frac{f_2^2 - f_1^2}{f_2^2 + f_1^2} \tag{6}$$

(f_1, f_2 are the resonance frequencies of the coupled pair of resonators), varies with respect to the permittivity/permeability of the substrate. This variation of the coupling coefficients is plotted in Fig. 3, which clearly shows that the stronger coupling corresponds to the glide scenario. It is also observed that the coupling has a combined electric/magnetic nature, with the magnetic coupling being slightly more significant. In similarity with [23], this combined
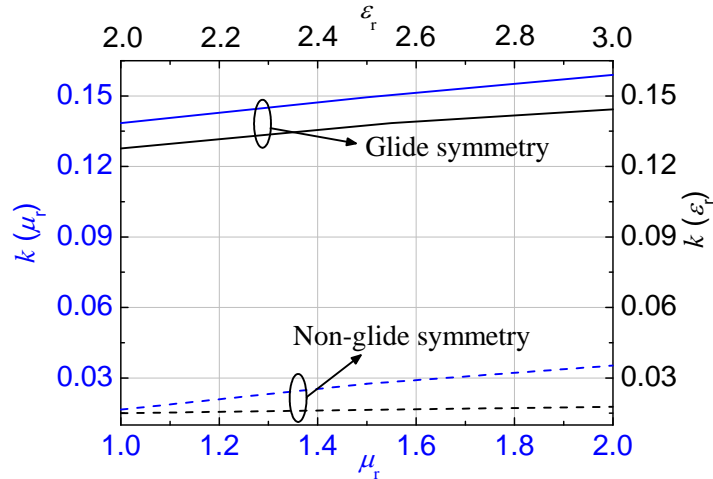
Fig. 3. Coupling factor (k) versus the relative permittivity (black lines) and permeability (blue lines) of the substrate.

coupling effect will approximately be accounted for by only the magnetic coupling k_R, as depicted with blue arrows in the equivalent circuits shown in Figs. 5(a) and 6(a).

B. Single CSRR etched on the SIW top wall

The first and simplest situation is a waveguide section of length $p = 5$ mm shown in Fig. 2(c), with a single CSRR etched on the top metallic wall. According to the above discussions, the proposed physically-based equivalent circuit for this structure is the one shown in Fig. 4(a), with the following values of the different elements taken from (1)–(4): $L_s = 1.71$ nH, $L_p = 16.7$ nH, and $C_p = 0.046$ pF with correcting factors $\xi_s = 1.09$ and $\xi_p = 1.64$. The magnetic coupling factor is $k_{RW} = 1$. The transmission response of this network is computed using the commercial software *ADS*, taking a value of impedance for the ports of $Z_p = 8400\,\Omega$ (this high impedance value should account for the evanescent nature of the waveguide sections). The circuit response is compared in Fig. 4(b) with simulations of the same structure obtained with *CST Microwave Studio*. An acceptable qualitative agreement can be observed for the frequency range where a bandpass behavior appears below the cutoff frequency of the SIW (the frequency range of interest in this work). This bandpass is well predicted by the simple equivalent circuit proposed and arises from the coupling of the CSRR resonator ($L_R C_R$ tank) with the different sections of the evanescent waveguide. Certainly, a further purely numerical tuning of the elements of the circuits can enhance the agreement with CST data in the considered frequency band. However, since in this work one of our goals is to gain as much physical insight as possible from the equivalent-circuit approach, we
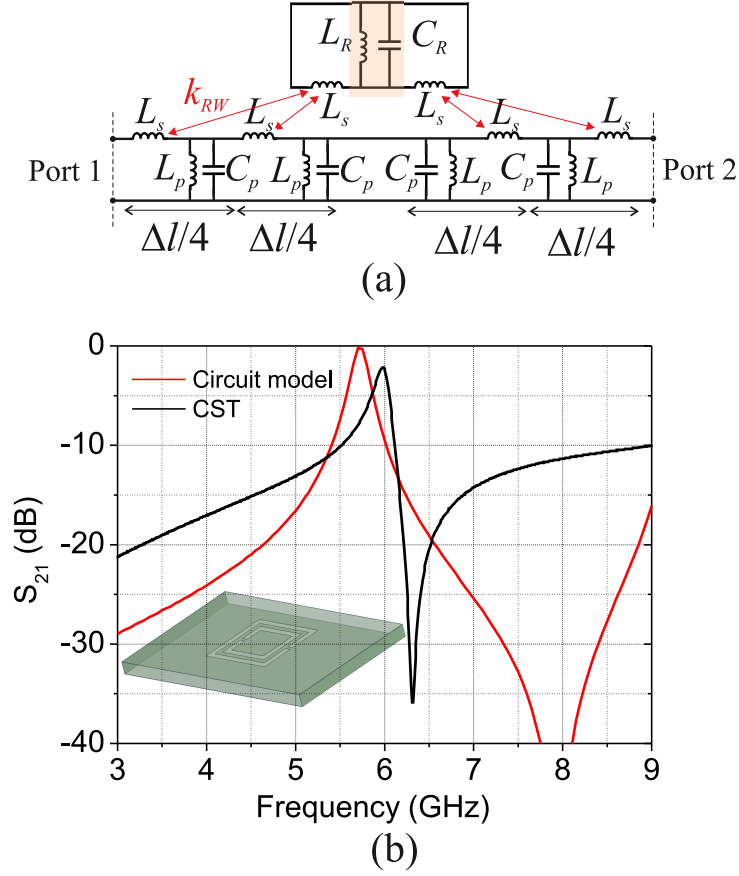
Fig. 4. (a) Equivalent circuit model of a rectangular waveguide section with one square CSRR etched on the top surface of the waveguide. (b) Response of the etched waveguide section of length Δl.

restrict ourselves to physically-based circuits with the minor possible *a posteriori* numerical fitting.

C. Two in-line CSRRs etched on the SIW top wall

In order to include the coupling effects between consecutive CSRRs in the structure shown in Fig. 5(b), we study the equivalent circuit model of a rectangular waveguide section of double length $\Delta l = 10\,\text{mm}$ with two in-line square CSRRs etched on the top waveguide wall (that is, two periods of the previously considered structure). The coupling of the resonators to the waveguide is again accounted for by the four inductive couplings shown in the corresponding equivalent circuit in Fig. 5(a) with red arrows and coupling factor k_{RW} while the magnetic coupling between the two in-line resonators is modeled by the coupling factor k_R with a blue arrow. The values of the different elements for this case are (L_R and C_R are the same as before): $L_s = 3.42\,\text{nH}$, $L_p = 8.35\,\text{nH}$, and $C_p = 0.092\,\text{pF}$. The correcting parameters in this case are $\xi_s = 1.09$ and $\xi_p = 1.64$. Convenient values for coupling coefficients are
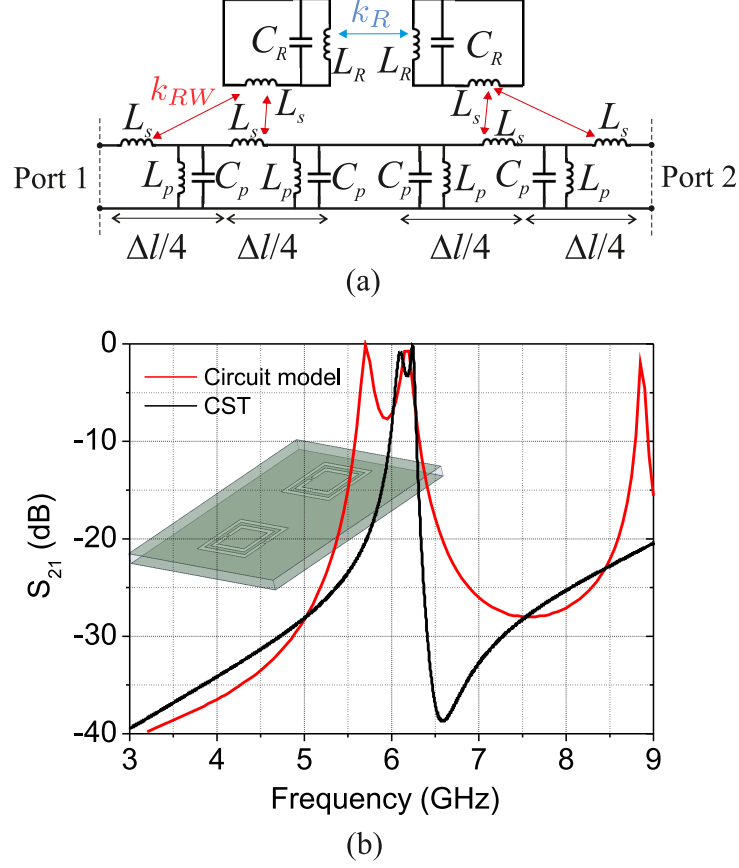
Fig. 5. (a) Equivalent circuit model of a rectangular waveguide section with two square CSRRs etched on the same waveguide surface. (b) Response of the etched waveguide section of length Δl.

found to be $k_{RW} = 1$ and $k_R = 0.46$. The transmission response of the present equivalent circuit is plotted in Fig. 5(b), showing a reasonable agreement with CST full-wave data. Due to the in-line magnetic coupling between CSRRs, the passband is now better defined and wider than in the previously analyzed single CSRR case.

D. Two CSRRs, etched separately on the SIW top and bottom walls

Finally, the equivalent circuit model of the glide-symmetric case is shown in Fig. 6(a), where the four-sections waveguide has a length of $\Delta l = 7.5$ mm. This structure corresponds to 1.5 periods of the initial structure but now with one CSRR in the top surface and another CSRR in the bottom surface and translated half period, where the added length takes into account the translation performed in the glide-symmetric case. The topology of the equivalent circuit is exactly the same as the previous non-glide case, except for the fact that the magnetic coupling between the two CSRRs is now *negative*; namely, $k_{RW} = 1$, $k_R = -0.46$. The values of the different elements for this case are: L_R and C_R as before, $L_s = 2.57$ nH, $L_p = 11.1$ nH
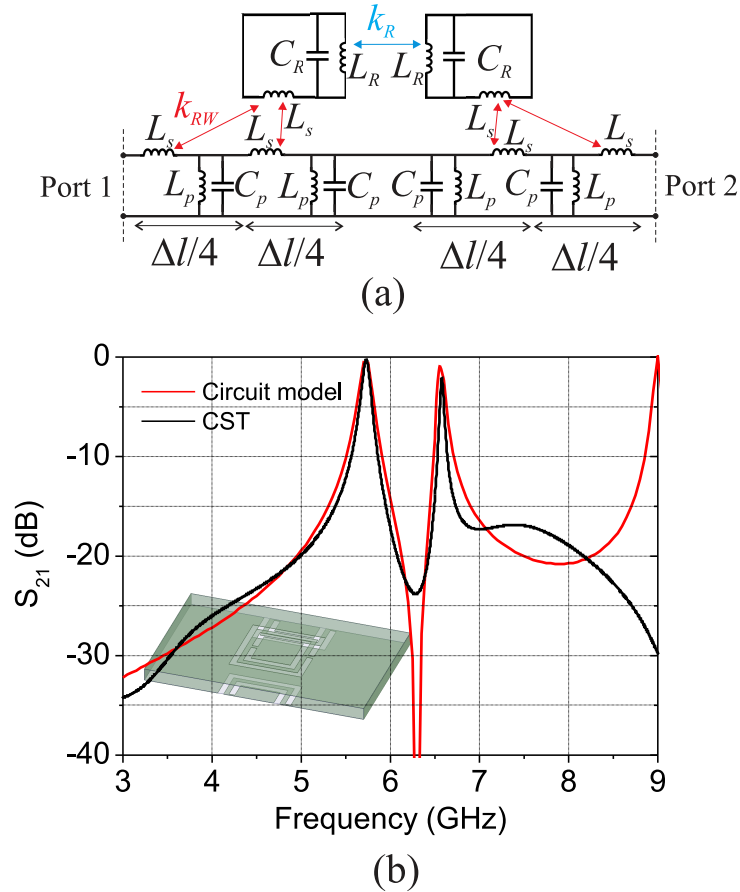
Fig. 6. (a) Equivalent circuit model of a rectangular waveguide section with two square CSRRs etched on the top and bottom waveguide surfaces. (b) Response of the etched waveguide section of length Δl.

and $C_p = 0.07\,\text{pF}$, which come from taking $\xi_s = 1.09$, and $\xi_p = 1.64$. The transmission response of the equivalent circuit is plotted in Fig. 6(b), showing now a good agreement with CST data. The figure reveals the presence of two resonances that are significantly more separated than in the previous non-glide symmetric case. This larger separation will be responsible for a wider passband when several unit cells are stacked.

In accordance with the discussion reported in [23], it is key to note here that the effect raised by the glide-symmetric disposition can be well accounted for by the same circuit used for the non-glide configuration but now simply changing the sign of the magnetic coupling between resonators. The key idea is that the resonators and waveguide sections are basically the same in the standard and the glide configurations. It means that self-inductance of the resonators is the same in both configurations. The only difference comes from the value of the mutual inductance, and specifically from a change of sign in this parameter. This change of sign is ultimately related to the location of the resonators since the mutual inductance between

two identical resonators (initially aligned vertically) changes from positive to negative as the horizontal distance between the resonators increases. It means that the mutual inductance in the glide configuration is expected to be negative. The widening of passband caused by changing the sign of the mutual inductance does not seem to have a direct and easy answer in the frame of circuit theory. In the present case, this widening is explained by the effect of the glide symmetry, as already reported and discussed in [8], [13].

This important information allows us to understand that the widening of the passband cannot only be achieved by increasing the magnitude of the magnetic coupling between resonators but also by changing the sign of this coupling. As shown with the present study case, a very simple and effective way of attaining this relevant change of sign turns out to be the use of glide symmetry in the filter geometry.

III. DISPERSION PROPERTIES

Once the equivalent-circuit approach has shed some physical insight into the underlying effects of the glide symmetry in our periodic structure, in order to characterize the electromagnetic field propagation of the periodic structures that will be used in the prototypes to be experimentally tested, the commercial software tool Ansys HFSS has been employed. The eigenmode module of such analysis tool yields the phase delay, $\phi = \beta p$, between its periodicity planes, with β being the modal phase constant. The cutoff frequencies of the modes of the periodic waveguide of unit cell p (see Fig. 1a) can be related to the frequency values where $\phi = 0$. An additional reason to use the full-wave simulator is that, in similarity with [25], we will include two rows of CSRRs etched on the top/bottom metallic surface of the SIW. The existence of a pair of CSRRs makes the corresponding equivalent circuit more complex because of the inductive couplings required to account for the additional couplings of the CSRRs with the waveguide as well as between the CSRRs themselves. In that situation, we would loose one of the basic advantages of the physically-based equivalent-circuit approach: the simplicity. As it is well known, we can always find an equivalent circuit that numerically fits the full-wave response in a given frequency band at the expense of loosing much of the expected physical insight provided by such equivalent circuit.

The structure under analysis in this section is shown in Fig. 1 and consists in a SIW of width $a_{\mathrm{SIW}} = 12.4\,\mathrm{mm}$ and height $b = 0.63\,\mathrm{mm}$ in which CSRRs have been periodically etched on the waveguide metallic walls. The selected substrate is Taconic RF-10 ($\varepsilon_r = 10$, $\tan\delta = 0.0025$), which thus yields a cutoff frequency of the initial SIW at about $4\,\mathrm{GHz}$. The vias defining the lateral walls of the SIW have diameter $d_s = 0.8\,\mathrm{mm}$ and separation
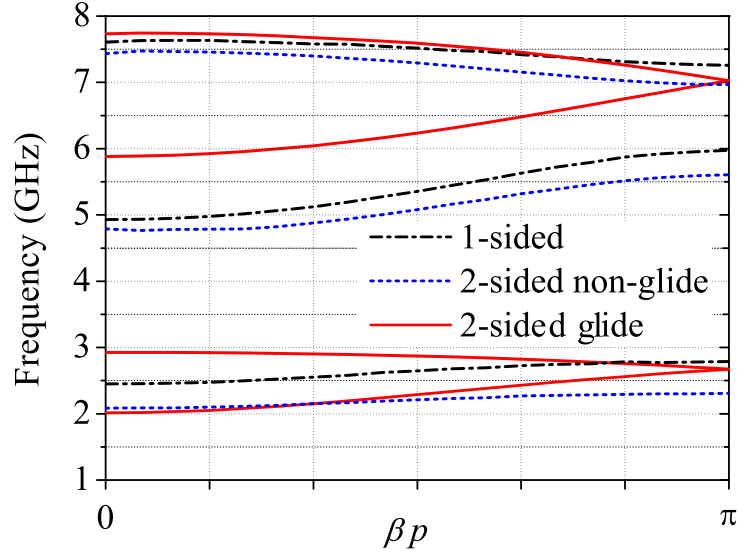
Fig. 7. Dispersion diagram of periodically CSRR-etched SIWs: Black line (1-sided) refers to a single array of etched CSRRs on the top waveguide wall. Blue line (2-sided non-glide) stands for the case where a pair of face-to-face arrays of CSRRs are etched on the top and bottom waveguide walls with no translation between them. Red line (2-sided glide) refers to the glide-symmetric configuration.

$s_v = 1.2$ mm, which guarantees negligible radiation losses. The geometrical parameters of the CSRRs in the unit cell are the same as those used in Sec. II. The substrate and dimensions have been chosen to achieve a low-frequency passband and a high level of compactness in the developed filters. Figs. 1(b,c) represent the unit cells without and with glide symmetry, respectively. In Fig. 1(b), the unit cell without glide symmetry has a pair of identical CSRRs etched on the top waveguide wall and centered in a waveguide section of length p with the bottom wall being a conventional metallic wall. Glide symmetry is created in Fig. 1(c) by also etching on the bottom waveguide surface the same CSRRs as the ones in the top surface, but translated $p/2$ along the waveguide axis (y-axis). The glide symmetry plane is normal to the z-axis, located in the middle of the substrate.

With the aid of the eigenmode module of Ansys HFSS, the dispersion diagram of the unit cells without and with glide symmetry shown in Figs. 1(b,c), along with the intermediate case of a non-glide two-sided etched structure, has been computed for a period of length $p =$ 7.55 mm. CSRRs etched on the bottom side also act as resonators. However, it should be clarified that, only when etching CSRRs on both waveguide walls in the glide configuration, an increase in bandwidth is found. This fact can be observed by comparing the blue and red curves in Fig. 7, which correspond to CSRR etched on both the top and bottom waveguide walls without and with glide symmetry. When the CSRRs are superimposed (i.e., non-glide

symmetric configuration, with blue line), the only effect with respect to the case of CSRRs etched only on the top wall (black line) is that the frequency of the passband decreases, but no increase of bandwidth is observed. This decrease in the passband is associated with a lower resonance frequency of the CSRRs, which can be explained if we see this structure as its equivalent case of a waveguide with half the height and CSRRs etched on the top waveguide wall. However, when glide symmetry is introduced, a clear increase of bandwidth is observed (red line). Thus, the glide symmetry effectively entails an increase of the filtering orders and strengthening of inter-resonator couplings. Plots in Fig. 7 also reveal that, in the non-glide configurations (both 1-sided and 2-sided cases), the propagation constant for the first modes (between 2 and 3 GHz) is highly dispersive. For the glide configuration (red lines), the first two modes are connected and their propagation constant is less dispersive, i.e., the bandpass is wider. Additionally, the second passband (second pair of modes) is pushed significantly to higher frequencies, thus resulting in a wider rejection band. These two properties are attractive for bandpass filters.

Fig. 8 shows the dispersion diagram of the first passband for the glide configuration analyzed in Fig. 7 for three different values of the period p. A direct observation from this figure shows that the lower the period, the wider the first passband of the structure, fact that can be attributed to a higher level of coupling between the unit cells. However, a very small value of p may lead to an extremely wide passband, which is not desirable for some practical applications, such as communications systems in which the bandwidth is often narrow. A convenient trade-off has to be considered for the specific application that is aimed to.

IV. Experimental validation

In order to demonstrate the enhanced characteristics of introducing glide symmetry in CSRR-based filters, a bandpass SIW filter has been designed with the same glide-symmetric unit cell analyzed in Sec. III, with 3 periodic cells; i.e., 3 pairs of CSRRs etched on the top surface of the SIW, and 3 pairs of CSRRs on the bottom surface, but translated $p/2$ in the waveguide axis.

Taper transitions from microstrip to SIW have been designed [32] and optimized. The design of the filter parameters for obtaining a desired frequency response (center frequency, bandwidth and rejection band) has been directly carried out from the information provided in Fig. 7, and only a final optimization process of the parameters of the taper transitions has been done. In the optimization process, we used the Quasi Newton (Gradient) Optimizer
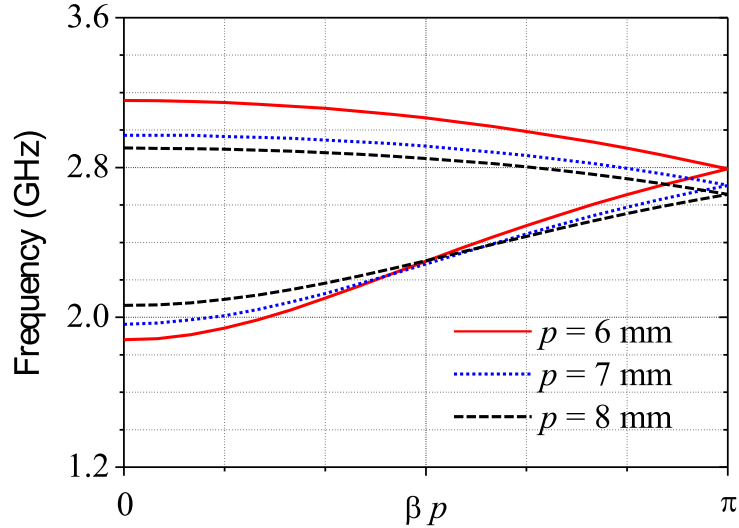
Fig. 8. Dispersion diagram of the two first modes of the periodic glide-symmetric configuration in Fig. 1(c), for different values of the period p.

provided by HFSS software). The optimized variables were w_t and l_t; i.e., the taper width and length, and we selected as cost function a S_{11} (dB) lower than -15 dB in the pass-band. The final parameters are: $a_{\text{SIW}} = 12.4$ mm, with period $p = 7.55$ mm, $w_t = 8.6$ mm, $l_t = 10.5$ mm, $w_m = 0.6$ mm, $l_g = 2.64$ cm, $l_T = 6.24$ cm, $l_{in} = 1.8$ mm, $l_{out} = 5.6$ mm, and $l_R = 7.94$ mm. The scheme of this filter is shown in Fig. 9(a), and photographs are provided in Fig. 9(b). The footprint area of the filter is $l_g \times a_{\text{SIW}} = 327.4$ mm^2.

The simulated electrical response of this glide-symmetric filter is represented in Fig. 10 with red lines, and it is compared to that of the same filter without glide-symmetry with black lines (i.e., an identical filter in which the bottom CSRRs have been removed). The S_{21} parameter of the original SIW is also represented in blue line for comparison purposes. In the glide-symetric case, 6 poles can be identified, yielding a much wider passband (defined at 10 dB input matching) from 2.2 to 2.86 GHz, in addition to a more extended rejection band, which extends up to 6 GHz. A narrower passband from 2.5 to 2.72 GHz is obtained in the corresponding non-glide symmetric filter configuration (showing only 3 poles in this case), along with a more reduced rejection band which extends up to 5 GHz. It can also be appreciated that the return losses in the passband are significantly lower in the glide-symmetric case (despite the optimization process carried out), given that a microstrip-to-SIW transition has been needed in order to get the filter response measured, and the wider passband of the glide configuration has been more difficult to match around 2.15 GHz [see the mismatch peak near the lower passband edge in Fig. 10]. However, it is important to remark that depending
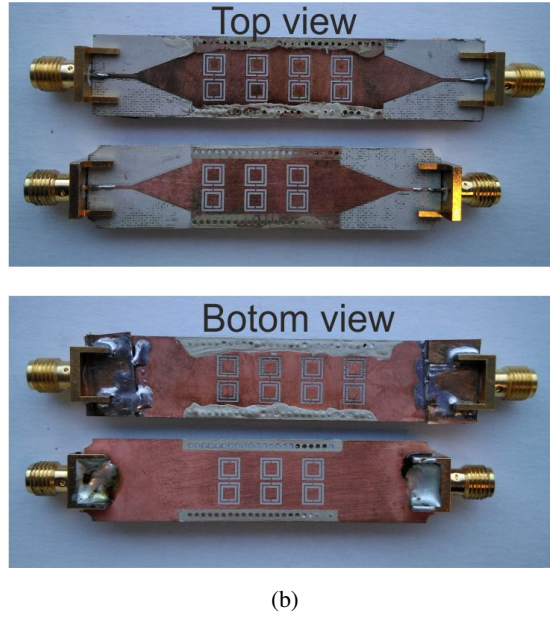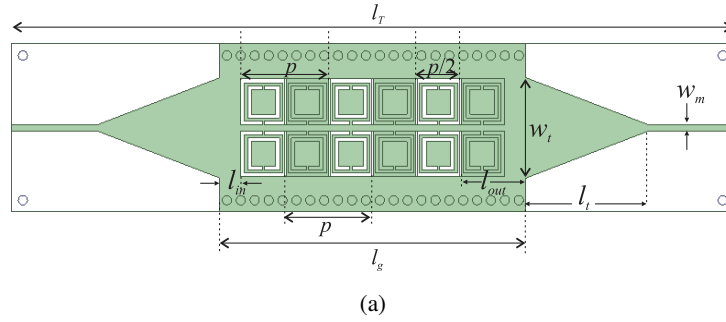
Fig. 9. (a) Scheme of the designed glide-symmetric filter. (b) Top and bottom views of the prototypes with 3 and 4 unit cells (a displacement of $p/2$ in the CSRR location can be observed in the bottom view).

on the final location of the filter in a practical system, the transition may not be required and thus the mismatch would be avoided. Insertion losses (IL) are significantly lower in the glide-symmetric filter configuration (lower than $1.8\,\mathrm{dB}$ from 2.2 to $2.6\,\mathrm{GHz}$), which is consistent with a wider passband. In order to check that there are not radiation losses in the resonators, the filter response has also been obtained without material losses (see the dotted lines in the figure inset in Fig. 10), showing that the insertion losses are very low in the pass-band (lower than 0.3 dB), or, equivalently, that the resonators are not radiating energy.

In order to check the resonant and coupling mechanisms between resonators, Fig. 11 shows the electric and magnetic field distribution in the periodic cell of the designed glide-symmetric filter at 2.37 GHz. At the selected phase, a high electric field intensity in the top resonators within the periodic cell is observed at this frequency while the magnetic field intensity is maximum in the area between them, thus revealing that the dominant coupling mechanism between the top and bottom resonators is of magnetic nature, as already predicted in Sec. II-A.
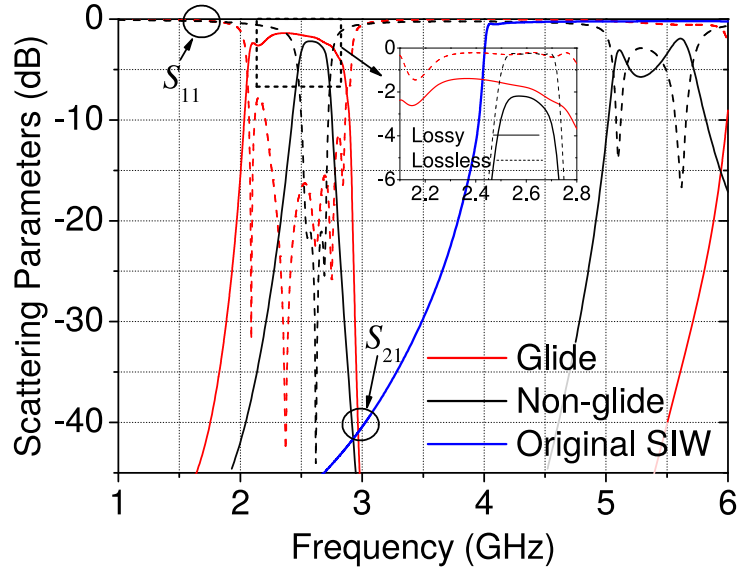
Fig. 10. Simulated electrical response ($|S_{21}|$: solid lines and $|S_{11}|$ dotted lines) of the designed glide-symmetric filter of Fig. 9 (red lines) along with the one of its equivalent non-glide symmetric filter (black lines). The $|S_{21}|$ parameter of the original SIW is also plotted (blue line) for comparison.
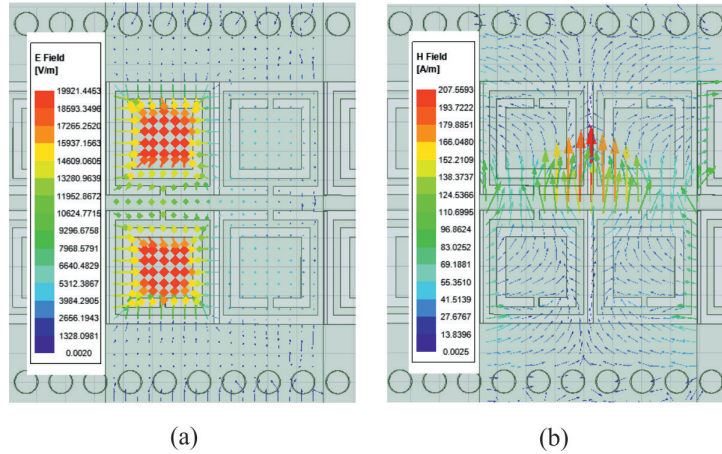

Fig. 11. (a) Electric and (b) magnetic field distribution in the periodic cell of the designed glide-symmetric filter at 2.37 GHz.

In Fig. 12, the measured response of the 3 unit cells glide-symmetric filter prototype is represented with red lines. The measured IL at the center frequency $f_0 = 2.5$ GHz is 2.4 dB, which is consistent with the 1.53 dB obtained in the simulation, being this difference attributed to the SMA-conector losses and to fabrication tolerances. Table I summarizes the performance characteristics of the proposed filter in this work and it is compared to conventional sub-wavelength CSRR-loaded SIW filters.

Finally, in order to experimentally determine the filter loss, an enlarged filter identical to
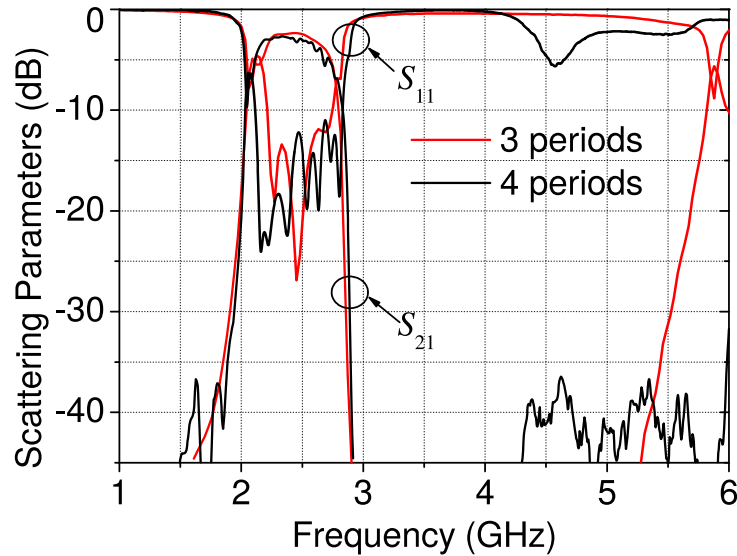
Fig. 12. Measured electrical response of the fabricated SIW filters with glide symmetry.

the previous one but with 4 unit cells has been fabricated, and its measured response has also been plotted in Fig. 12 with black lines, showing slightly higher ILs in the passband. In this figure, it can also be observed a higher number of poles with respect to the previous fabricated filter of 3 unit cells, which is consistent with a higher number of resonators, although the pass-band is almost unchanged. The loss difference between the 3 and 4 unit cells prototypes as a function of frequency is represented in Fig. 13 with black crosses. This graph represents only the frequency range with $10\,\mathrm{dB}$ input matching, which goes from 2.21 to $2.75\,\mathrm{GHz}$. A linear fitting of the IL difference is represented in red. A mean insertion loss difference of $0.5\,\mathrm{dB}$ is observed in the passband of the filter, which results in a value of $2.5\ \mathrm{dB}/\lambda_\epsilon$. Our experiments show a clear improvement in bandwidth and insertion losses with respect to similar sub-wavelength filter topologies reported in the technical literature that employ resonators to produce evanescent wave transmission (see Table I). All the miniaturized filters that operate below cut-off are narrowband and have higher insertion losses than conventional filters. Our goal here was to reduce the level of losses while compressing the transversal dimension of the waveguide. This transversal compression is crucial in practical applications; for example, in communications systems where the space to feed antenna arrays is limited. Therefore, to have waveguides that operate below the cut-off frequency is needed to reduce the levels of grating lobes.

TABLE I

COMPARISON OF PERFORMANCE OF THIS WORK WITH OTHER SUB-WAVELENGTH FILTER TOPOLOGIES

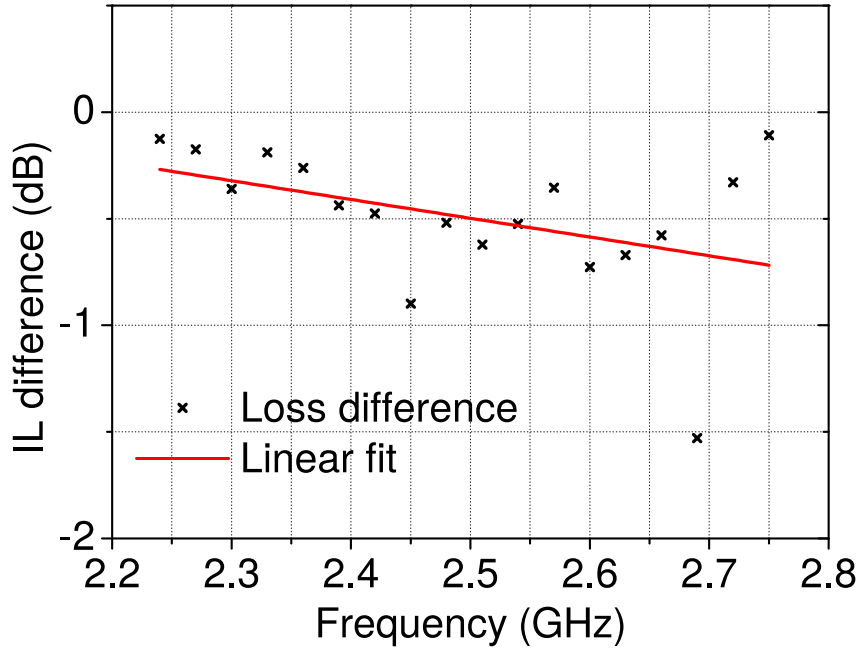|	Number of CSRRs	Center freq. (GHz)	FBW (%)	Minimum IL (dB)	Minimum RL (dB)	Size (mm^2)
[33]	10	5.45	3.43	5.8	> 10	442.26
[34]	4	2.4	10	4.5	8	875
[35]	3	1.6	20	4.5	> 10	100
This work	12	2.5	24	2.4	> 10	327.4

*FBW: Fractional Bandwidth

Fig. 13. Comparison of the filter losses in the passband as a function of frequency.

V. CONCLUSION

Here, we have demonstrated that glide symmetry modifies the dispersion properties of a SIW loaded periodically with CSRR. In particular, glide symmetry reduces the dispersion of the first propagative mode, and increases the bandwidth of the stopband between the first and second pair of modes. This effect has been explained with a circuit model in which the coupling between elements plays a key role. In the case of glide symmetry, the magnetic coupling is *negative*, strongly modifying the properties of the periodic structure. The opportunities of the proposed structure are demonstrated with an example which has been experimentally tested. In this example, propagation below the cutoff has been evidenced with

an enhanced bandwidth and reduced losses when compared to the case of a conventional unit cell. As a general conclusion, it can be stated that the results of this work show that glide symmetry can easily be complemented with other design strategies in SIW technology to enhance different performance characteristics.

ACKNOWLEDGEMENT

REFERENCES

[1] Y.-C. Chen, C.-C. Tzuang, T. Itoh, and T. K. Sarkar, "Modal characteristics of planar transmission lines with periodical perturbations: their behaviors in bound, stopband, and radiation regions," *IEEE Trans. Antennas Propag.*, vol. 53, no. 1, pp. 47–58, Jan 2005.

[2] S. Hrabar, J. Bartolic, and Z. Sipus, "Waveguide miniaturization using uniaxial negative permeability metamaterial," *IEEE Trans. Antennas Propag.*, vol. 53, no. 1, pp. 110–119, Jan 2005.

[3] I. A. Eshrah, A. A. Kishk, A. B. Yakovlev, and A. W. Glisson, "Rectangular waveguide with dielectric-filled corrugations supporting backward waves," *IEEE Trans. Microw. Theory Techn.*, vol. 53, no. 11, pp. 3298–3304, Nov 2005.

[4] R. Rodriguez-Berral, F. Mesa, P. Baccarelli, and P. Burghignoli, "Excitation of a periodic microstrip line by an aperiodic delta-gap source," *IEEE Antennas Wireless Propag. Lett.*, vol. 8, pp. 641–644, 2009.

[5] H. Zhu and J. Mao, "Miniaturized tapered EBG structure with wide stopband and flat passband," *IEEE Antennas Wireless Propag. Lett.*, vol. 11, pp. 314–317, 2012.

[6] P. J. Crepeau and P. R. McIsaac, "Consequences of symmetry in periodic structures," *Proc. IEEE*, vol. 52, no. 1, pp. 33–43, Jan 1964.

[7] A. Hessel, M. H. Chen, R. C. M. Li, and A. A. Oliner, "Propagation in periodically loaded waveguides with higher symmetries," *Proc. IEE*, vol. 61, no. 2, pp. 183–195, Feb 1973.

[8] G. Valerio, F. Ghasemifard, Z. Sipus, and O. Quevedo-Teruel, "Glide-symmetric all-metal holey metasurfaces for low-dispersive artificial materials: Modeling and properties," *IEEE Trans. Microw. Theory Techn.*, vol. 66, no. 7, pp. 3210–3223, July 2018.

[9] O. Quevedo-Teruel, M. Ebrahimpouri, and M. N. M. Kehn, "Ultrawideband metasurface lenses based on off-shifted opposite layers," *IEEE Antennas Wireless Propag. Lett.*, vol. 15, pp. 484–487, Dec 2016.

[10] O. Quevedo-Teruel, J. Miao, M. Mattsson, A. Algaba-Brazalez, M. Johansson, and L. Manholm, "Glide-symmetric fully metallic Luneburg lens for 5G communications at Ka-band," *IEEE Antennas Wireless Propag. Lett.*, vol. 17, no. 9, pp. 1588–1592, Sept 2018.

[11] T. Chang, J. U. Kim, S. K. Kang, H. Kim, D. K. Kim, Y.-H. Lee, and J. Shin, "Broadband giant-refractive-index material based on mesoscopic space-filling curves," *Nature Commun.*, vol. 7, Article number 12661, 2016.

[12] D. Cavallo and C. Felita, "Analytical formulas for artificial dielectrics with nonaligned layers," *IEEE Trans. Antennas Propag.*, vol. 65, no. 10, pp. 5303–5311, Oct 2017.

[13] M. Ebrahimpouri, O. Quevedo-Teruel, and E. Rajo-Iglesias, "Design guidelines for gap waveguide technology based on glide-symmetric holey structures," *IEEE Microw. Wireless Compon. Lett.*, vol. 27, no. 6, pp. 542–544, June 2017.

[14] H. Meng, D. Chronopoulos, A. T. Fabro, W. Elmadih, and I. Maskery, "Rainbow metamaterials for broadband multi-frequency vibration attenuation: Numerical analysis and experimental validation," *J. Sound Vib.*, vol. 465, p. 115005, Jan 2020.

[15] P. Celli, B. Yousefzadeh, C. Daraio, and S. Gonella, "Bandgap widening by disorder in rainbow metamaterials," *App. Phys. Lett.*, vol. 114, no. 9, p. 091903, March 2019.

[16] M. Ebrahimpouri, E. Rajo-Iglesias, Z. Sipus, and O. Quevedo-Teruel, "Cost-effective gap waveguide technology based on glide-symmetric holey EBG structures," *IEEE Trans. Microw. Theory Techn.*, vol. 66, no. 2, pp. 927–934, Feb 2018.

[17] A. Vosoogh, H. Zirath, and Z. S. He, "Novel air-filled waveguide transmission line based on multilayer thin metal plates," *IEEE Trans. THz Sci. Technol.*, vol. 9, no. 3, pp. 282–290, May 2019.

[18] M. Ebrahimpouri, A. A. Brazalez, L. Manholm, and O. Quevedo-Teruel, "Using glide-symmetric holes to reduce leakage between waveguide flanges," *IEEE Microw. Wireless Compon. Lett.*, vol. 28, no. 6, pp. 473–475, June 2018.

[19] A. Monje-Real, N. J. G. Fonseca, O. Zetterstrom, E. Pucci, and O. Quevedo-Teruel, "Holey glide-symmetric filters for 5G at millimeter-wave frequencies," *IEEE Microw. Wireless Compon. Lett.*, vol. 30, no. 1, pp. 31–34, Jan 2020.

[20] M. Ebrahimpouri and O. Quevedo-Teruel, "Ultrawideband anisotropic glide-symmetric metasurfaces," *IEEE Antennas Wireless Propag. Lett.*, vol. 18, no. 8, pp. 1547–1551, Aug 2019.

[21] M. Ebrahimpouri, L. F. Herran, and O. Quevedo-Teruel, "Wide-angle impedance matching using glide-symmetric metasurfaces," *IEEE Microw. Wireless Compon. Lett.*, vol. 30, no. 1, pp. 8–11, Jan 2020.

[22] M. Bagheriasl, O. Quevedo-Teruel, and G. Valerio, "Bloch analysis of artificial lines and surfaces exhibiting glide symmetry," *IEEE Trans. Microw. Theory Techn.*, vol. 67, no. 7, July 2019.

[23] B. A. Mouris, A. Fernández-Prieto, R. Thobaben, J. Martel, F. Mesa, and O. Quevedo-Teruel, "On the increment of the bandwidth of mushroom-type ebg structures with glide symmetry," *IEEE Trans. Microw. Theory Techn.*, vol. 68, no. 4, pp. 1365–1375, April 2020.

[24] J. D. Baena, J. Bonache, F. Martin, R. M. Sillero, F. Falcone, T. Lopetegi, M. A. G. Laso, J. Garcia-Garcia, I. Gil, M. F. Portillo, and M. Sorolla, "Equivalent-circuit models for split-ring resonators and complementary split-ring resonators coupled to planar transmission lines," *IEEE Trans. Microw. Theory Techn.*, vol. 53, no. 4, pp. 1451–1461, April 2005.

[25] Y. D. Dong, T. Yang, and T. Itoh, "Substrate integrated waveguide loaded by complementary split-ring resonators and its applications to miniaturized waveguide filters," *IEEE Trans. Microw. Theory Techn.*, vol. 57, no. 9, pp. 2211–2223, Sept. 2009.

[26] F. Martin, *Artificial Transmission Lines for RF and Microwave Applications*. John Wiley & Sons, Ltd, 2015.

[27] Y. Cassivi, L. Perregrini, P. Arcioni, M. Bressan, K. Wu, and G. Conciauro, "Dispersion characteristics of substrate integrated rectangular waveguide," *IEEE Microw. Wireless Compon. Lett.*, vol. 12, no. 9, pp. 333–335, Sept. 2002.

[28] J. Martínez, A. Coves, E. Bronchalo, A. A. S. Blas, and M. Bozzi, "Band-pass filters based on periodic structures in SIW technology," *AEU Int. J. Electron. Commun.*, vol. 112, p. 152942, 2019.

[29] N. Marcuvitz, *Waveguide Handbook*. Isha Books, 2013.

[30] C. C. Johnson, *Field and Wave Electrodynamics*. MacGraw-Hill Book Company, 1965.

[31] J. Hong and M. Lancaster, *Microstrip Filters for RF / Microwave Applications*, ser. Wiley Series in Microwave and Optical Engineering. Wiley, 2001.

[32] D. Deslandes and K. Wu, "Integrated microstrip and rectangular waveguide in planar form," *IEEE Microw. Wireless Compon. Lett.*, vol. 11, no. 2, pp. 68–70, 2001.

[33] Y. Dan, T. Yang, and T. Itoh, "Substrate integrated waveguide loaded by complementary split-ring resonators and its

applications to miniaturized waveguide filters," *IEEE Trans. Microw. Theory Techn.*, vol. 57, no. 9, pp. 2211–2223, Sept 2009.

[34] J. García-García, J. Bonache, I. Gil, F. Martín, M. Velázquez-Ahumada, and J. Martel, "Miniaturized microstrip and cpw filters using coupled metamaterial resonators," *IEEE Trans. Microw. Theory Techn.*, vol. 54, no. 6, pp. 2628–2635, June 2006.

[35] J. Bonache, M. Gil, I. Gil, J. García-García, and F. Martín, "Limitations and solutions of resonant-type metamaterial transmission lines for filter applications: The hybrid approach," in *Proc. IEEE MTT-S Int. Microw. Symp. Dig.*, June 2006, p. 939–942.